# Aeroelastic Modelling of Highly Flexible Wings

C. Howcroft*, R.G. Cook*, D. Calderon*, L. Lambert*,
M. Castellani*, J.E. Cooper*, M.H. Lowenberg*, S.A. Neild* and E. Coetzee†

**This paper details five aeroelastic modelling methods applied to the study of an example high aspect ratio wing subject to high loads resulting in large structural deformations. Each method is discussed in turn and example static results from each are compared. Overall agreement is illustrated between the methods for key quantities of interest although aerodynamic modelling choices regarding the orientation of aero forces is observed to play a significant role in the agreement between predicted distributed loads and deflections. Quantitative differences resulting from linearisation of the wing model are also presented and discussed. It is found that by linearising the problem, wing deflection, aerodynamic forces and root bending are all over-estimated. Large differences are also observed between linear and nonlinear predictions of root twist, however the modelling of drag effects is deemed important to the exact nature of the observed discrepancy. Altogether, linearised assumptions are shown to have a noticeable impact on the accuracy of predicted results for the considered wing test case and are deemed unsuitable in isolation for the analysis of this class of flexible problem.**

## I. Introduction

High aspect ratio wings can lead to significant fuel savings due to increased aerodynamic efficiency, primarily because of the reduction in induced drag. The drive toward Natural Laminar Flow wings has also renewed the interest in higher aspect ratio low swept wings. However, such designs are also often prone to larger bending moments necessitating the addition of structural weight. Furthermore, such designs have little or no sweep and therefore the gust load alleviation benefit due to bending-torsion coupling inherent in swept-back designs is absent. High aspect ratio highly flexible wings are notoriously prone to nonlinear aeroelastic instabilities, and these nonlinear effects are usually not well understood; therefore, the wing is stiffened to avoid such instabilities, again with the penalty of additional structural weight.

Figure 1: Airbus[1] and Boeing[3,21] examples of concept aircraft with high aspect ratio wings

Despite the potential drawbacks of such designs a number of high aspect ratio wing configurations are being considered, and both Airbus and Boeing have published their own concepts, as shown in figure 1. The Boeing SUGAR Volt aircraft[3,18,21] has a 51.8 m wing span, an aspect ratio of 19.55 and includes a strut to prevent

*Department of Aerospace Engineering, University of Bristol, Queen's Building, University Walk, Bristol BS8 1TR.
†Future Projects Office, Airbus Operations Ltd, Pegasus House Aerospace Avenue, Filton, Bristol BS34 7PA.

the need of additional structural weight in tackling the large bending loads; however, this may also lead to extra drag. The small sweep of this designs results in a lower cruise speed to help avoid wave drag; drag is also mitigated by reducing the thickness to chord ratio of the slender wing. Overall such a configuration enables laminar flow over a greater proportion of the wing, but also increase structural flexibility and the potential for aeroelastic instability.[3]

In the case of high-altitude long-endurance (HALE) aircraft, ultra low structural weight and aerodynamic efficiency are critical to their design and so the wings are inherently flexible. Examples include the NASA Helios and Boeing SolarEagle concepts. Large geometric deformations are commonplace, which naturally test the limits of linear theory in the design. However the ability to model such flexible configurations in the conceptual design stage is essential for the calculation of limit loads, and consequently, structural sizing. For conventional aircraft, this type of modelling is common practice and relatively straightforward, as airframe manufacturers usually have both commercial and in-house software at their disposal. However, such modelling techniques are not necessarily sufficient to capture the nonlinearities that are characteristic of unconventional, high-aspect-ratio configurations. Software or tools that are capable of modelling these nonlinear effects are not readily available, making it difficult to reliably determine the benefits and limitations of new configurations.

This paper details a suite of nonlinear modelling strategies capable of analysing such configurations, thus pointing the way towards removing some of the obstacles that currently prevent the robust design of highly flexible wing configurations. In section II each of these models is introduced in turn. The potential benefits of each are discussed and constituent equations detailed where appropriate. Section II.G discusses the aerodynamic implementation coupled to each of these structural methods and details the specific geometric application of aerodynamic forces. In section III comparative results are plotted for a series of static test cases. Results are divided into tip load cases (§III.A), spanwise distributions for fixed root angles of attack (§III.B.1) and aeroelastic trends as root $\alpha$ is varied (§III.B.2). The section finishes with a brief forward look to the potential impact of drag modelling and in section IV conclusions are drawn from the study.

## II. Overview of Modelling Techniques

### II.A. Wing Model

The wing model considered for this report is based on the high aspect ratio aircraft treated in the study of Patil et al.[17] This full aircraft exhibits sufficient structural flexibility to form a suitable geometrically nonlinear test case on which to base the comparative analyses of this study. The full aircraft has a un-swept configuration of 32m span with rectangular planform (chord = 1m). The wings are uncambered with zero initial twist and zero dihedral; the wing cross-sectional profile comprises a NACA0012 aerofoil from root to tip. The test case treated in this report considers the clamped half wing from this aircraft as illustrated in figure 2.

Specific parameters pertaining to this wing model are given in table 1. This parameter set defines a wing with a high degree of flexibility and thus necessitates the use of methods capable of capturing the resultant geometric nonlinearity. The five modelling methods introduced in the following sections seek to model the static behaviour of this system. Each take a 1D beam representation of the wing and are all capable of representing arbitrarily large nonlinear structural deflections.

### II.B. Nonlinear Iterative Method Using MSC Nastran

The need for validation is one of the major issues faced when developing new methods for analysing high-aspect-ratio wings that are geometrically nonlinear. A wide range of research in aeroelastic analysis has been validated using the commercial software, MSC Nastran, which is extremely reliable and enables high-fidelity structural analysis. However, all of the native Nastran aeroelastic analysis modules are limited to structures that behave linearly. This poses a problem if one wishes to reliably determine the static aeroelastic behaviour of a high-aspect-ratio aircraft, because many of the assumptions that Nastran makes are invalid for these

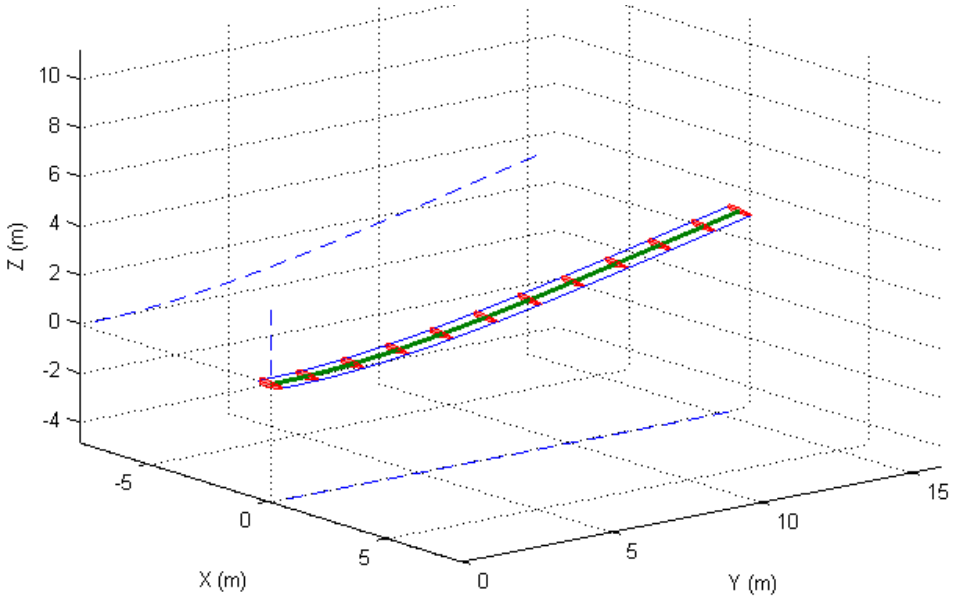


Figure 2: Wing geometry for an example deflection given for $\alpha_{root} = 2$ degrees; flight condition given in table 1. The coordinate origin is placed on the beam axis at the root mid-chord position.

| Wing Geometric Properties | |
|---|---|
| Semi-span $(m)$ | 16 |
| Chord $(m)$ | 1 |
| Taper ratio | 1 |
| 1/4 chord sweep $(^\circ)$ | 0 |
| Dihedral $(^\circ)$ | 0 |
| **Wing Structural Properties** | |
| Mass per unit length $(kg/m)$ | 0.75 |
| In-Plane Bending Stiffness, $EI_{xx}$ $(Nm^2)$ | $2 \times 10^4$ |
| Out-of-Plane Bending Stiffness, $EI_{zz}$ $(Nm^2)$ | $4 \times 10^6$ |
| Torsional Stiffness, $GJ$ $(Nm/rad)$ | $1 \times 10^4$ |
| **Flight Condition** | |
| Airspeed $(m/s)$ | 30 |
| Air density $(kg/m^3)$ | 0.0881 |
| Mach No. | 0.1017 |
| Altitude $(ft)$ | 20000 |

Table 1: Geometric properties of the wing model.[17]

wings. For example, the assumption of small displacements is not true for highly flexible wings that are subject to a large load such as a limit gust load or high g manoeuvre.

In a standard Nastran flexible trim analysis, the aerodynamic loads on an aircraft are computed using a doublet lattice method (DLM) solver and updated based on the trim conditions and the deformed shapes of the lifting surfaces, which are determined from linear structural analysis. These loads are then used to determine the final deformed shape of the aircraft, assuming linear displacements. All of this occurs within the 'black box' of the static aeroelasticity module (SOL 144) so the procedure, illustrated in Figure 3, is very simple.
Although the aeroelastic modules only include linear structural analyses, Nastran does have the capability

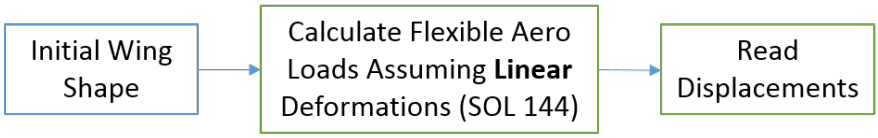


Figure 3: Procedure for the linear method.

to perform a separate nonlinear structural analysis using the SOL 106 module. One way to account for the limitations of Nastran is to extract the aerodynamic forces from a standard flexible trim analysis (SOL 144) and apply them to the structure in a separate nonlinear structural analysis. This approach, illustrated in Figure 4, is commonly used to model the aeroelastic behaviour of geometrically nonlinear aircraft. For example, recent research from the project Subsonic Ultra Green Aircraft Research (SUGAR) Project, known as SugarVolt[3,21] uses a quasi-nonlinear aeroelastic analysis to compute flutter speeds by obtaining the pre-stressed mode shapes based on the results of a nonlinear static analysis. The quasi-nonlinear descriptor is employed here as the method obtains the aerodynamic distribution from a linear aero-elastic analysis and applies this to a subsequent nonlinear static analysis. This method is summarised by the flow process of Figure 4.

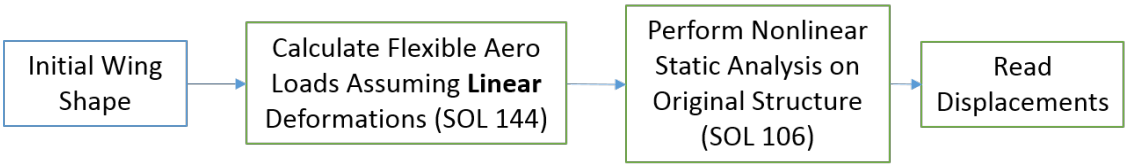


Figure 4: Procedure for the quasi-nonlinear method

In order to expand upon the quasi-nonlinear 'SugarVolt' method and capture the stronger nonlinear effects present for the wing of this study an alternative method is introduced here, termed the Nonlinear Iterative Method. This method still has the benefits of using Nastran, but does not assume that the displacements are linear when calculating the aerodynamic loads. The iterative procedure (Figure 5), which is controlled using MatLab, only uses the Nastran SOL 144 aeroelastic module to calculate the *rigid* aerodynamic loads and performs all of the structural analysis using the SOL 106 nonlinear structural module. A new aerodynamic mesh is created in every loop, based on the nonlinear displacements, so that new loads can be calculated. The process is repeated until the wing displacement converges to that of the previous iteration. Even though a rigid trim analysis is carried out within the SOL 144 module, the overall analysis is a nonlinear flexible trim due to the inclusion of nonlinear displacements outside the SOL 144 'black box.' This type of analysis can be performed on a full free-free aircraft or on a wing that is fixed at the root.

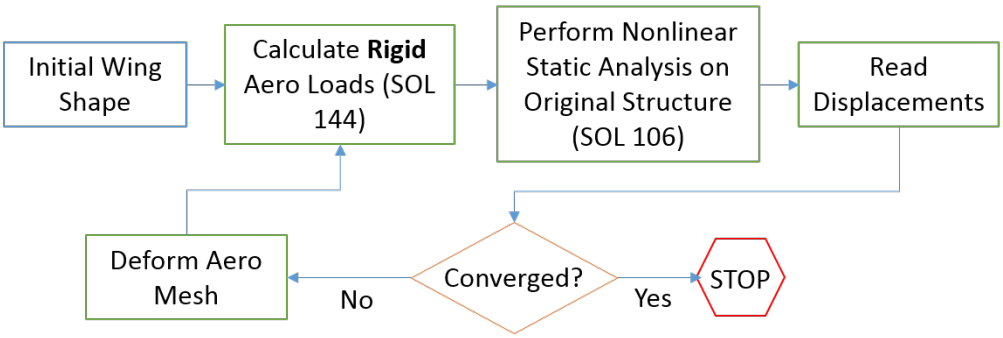


Figure 5: Procedure for the nonlinear iterative method.

One of the key points of this method is that, by updating the orientation of the aerodynamic mesh in every loop, it captures the fact that aerodynamic loads are not always vertical, but follow the deformed shape of the lifting surfaces. This effect significantly alters the lift distribution because, for very flexible aircraft,

the inboard component of the aerodynamic force is not negligible. An example of the difference between the lift distributions of each method is shown in Figures 6 (note, the linear results is hidden behind the quasi-nonlinear curve).

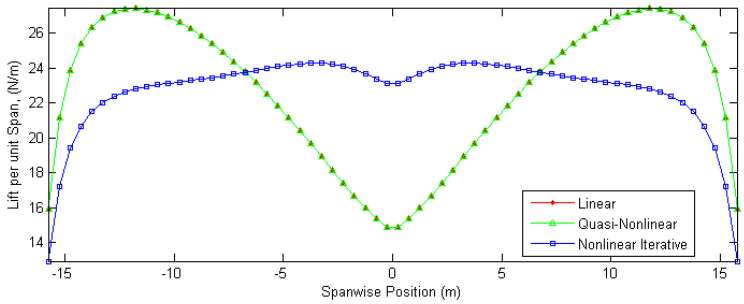


Figure 6: Linear, quasi-nonlinear and nonlinear iterative lift distribution.

The differences between the methods outlined above have a significant impact when determining the static aeroelastic behaviour of flexible aircraft such as that considered in this paper. One example, showing the deformed shape of a very flexible wing under a 1.0g load, is given in Figure 7 for the HALE aircraft,[17] see section II.A.

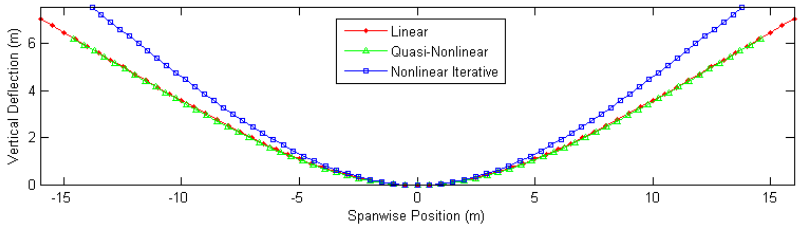


Figure 7: Deformed shape of HALE wing using different methods.

Figure 7 shows that when geometric structural nonlinearity is fully accounted for, the deformation of the wings can deviate substantially from the linear and quasi-nonlinear cases; in addition to visible differences in the magnitude of deflection, one notes that tip shortening effects when retaining a constant beam length are also neglected from the linear/quasi-linear methods. Altogether, this means that currently accepted methodologies for modelling nonlinear aeroelastic problems require adaptation to produce robust designs and gain insight into the behaviour of unconventional flexible aircraft.

## II.C. NeoCASS

NeoCASS (Next generation Conceptual Aero-Structural Sizing Suite) provides a design framework developed at the Department of Aerospace Engineering of Politecnico de Milano. The program is divided into two parts, GUESS (Generic Unknowns Estimator in Structural Sizing) and SMARTCAD (Simplified Models for Aeroelasticity in Conceptual Aircraft Design). This paper takes advantage of the nonlinear beam formulation used in these packages to model the geometric nonlinearities of a highly deflected wing. For further details of this suite please refer to Cavagna.[6]

### *II.C.1. Beam Formulation*

A brief description of the beam formulation used in NeoCASS is provided in this section; more detail can be found in.[6,10] A three-node linear/nonlinear finite-volume beam (see figure 8) is implemented, the formulation of which was originally proposed by Ghiringelli, and proved to be intrinsically shear-lock free.

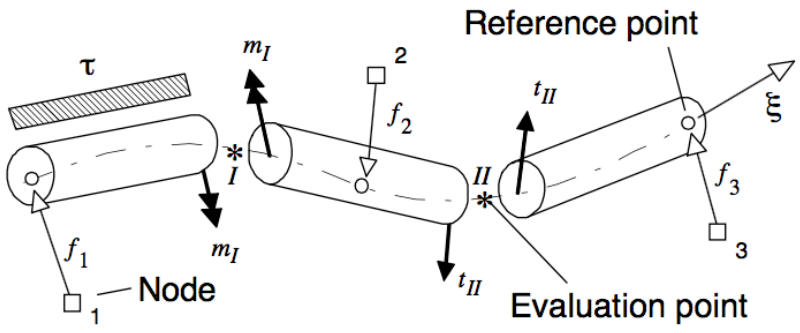


Figure 8: Three-nodel linear/nonlinear finite-volume beam

The finite volume approach describes the equilibrium of internal forces and external loads for a finite piece of beam. The points that bound the piece of beam are described as *evaluation* points since the internal forces need only be evaluated at these two locations. In the linear case, the formulation leads to the exact solution for end applied loads given an appropriate choice of points. The three parts of the beam are related to reference points along the beam which are in turn related to the geometrical nodes through an offset $f$ (see figure 8), allowing for disparities between the elastic axis and the centre of mass. Each node is described by a position vector of translation and rotational components, $x = [x_i, \psi_i]$, and a rotation matrix, $R(g)$, expressed by the Gibb-Rodriguez rotation parameters $g$, so that for each node, $p_i = x_i + Rf_i$. Independent parabolic shape functions $N(\xi)(1/2\xi(\xi-1)\ ,\ 1-\xi^2\ ,\ 1/2\xi(\xi+1))$ are used to recover the position of an arbitrary point $(p(\xi))$ along the reference line. The evaluation points are placed at $\xi = \pm 1/\sqrt{3}$. Generalised strains and curvatures are based on an intrinsic formulation of the beam. The node equilibrium equations take on the following form:

$$\mathcal{A}\Theta = \mathcal{F} \tag{1}$$

where $\mathcal{A}$ describes the *moment arm* matrix, $\Theta$ the internal generalised forces and $\mathcal{F}$ is the vector of external generalised loads.

The matrix $\mathcal{A}$ originates from the finite equilibrium equation. $p_I$ and $p_{II}$ are the evaluation points.

$$\mathcal{A} = \begin{pmatrix} -I & 0 & 0 & 0 \\ (p_I - p_1)_X & -I & 0 & 0 \\ -I & 0 & -I & 0 \\ -(p_I - p_2)_X & I & -(p_{II} - p_2)_X & -I \\ 0 & 0 & I & 0 \\ 0 & 0 & -(p_{II} - p_3)_X & I \end{pmatrix} \tag{2}$$

The sub-script $*_X$ denotes the skew-symmetric cross product operator formed from the elements of the vector quantity in question. $\Theta$ consists of nodal forces and moments resolved in the global reference frame for each evaluation point. These are recovered by rotating the forces from the material reference frame which are related to the strains and curvatures through a sectional stiffness matrix at the two evaluation points. So that $\Theta = \mathcal{R}\tilde{\mathcal{D}}\mathcal{R}^T\Psi$, where $\mathcal{R}$ is a block diagonal of rotation matrices for each evaluation point, $\tilde{\mathcal{D}}$ is the sectional stiffness matrix and $\Psi = \begin{Bmatrix} \epsilon_I & \kappa_I & \epsilon_{II} & \kappa_{II} \end{Bmatrix}$ is the vector of generalised strains and curvatures in the global reference frame. The strains and curvatures are defined as follows:

$$\epsilon = p' + p'_{0X}\varphi \tag{3}$$

$$\kappa = \varphi' \tag{4}$$

where $p_0$ is the initial reference line. When discretised this becomes:

$$\epsilon = N_i' x_i + p_{0X}' N_i \varphi_i - N_i' f_{iX} \varphi_i \tag{5}$$

$$\kappa = N_i' \varphi_i \tag{6}$$

The finite equilibrium equation is then written as:

$$\mathcal{A}\mathcal{R}\tilde{\mathcal{D}}\mathcal{R}^T \begin{bmatrix} N_{Ii}' & p_{0IX}' N_{Ii} - N_{Ii}' f_{iX} \\ 0 & N_{Ii}' \\ N_{IIi}' & p_{0IIX}' N_{IIi} - N_{IIi}' f_{iX} \\ 0 & N_{IIi}' \end{bmatrix} \begin{Bmatrix} x_i \\ \varphi_i \end{Bmatrix} = \mathcal{F} \tag{7}$$

### *II.C.2. Static Aeroelastic Analysis*

The nonlinear aeroelastic solver takes on a very similar approach to the one implemented by the Nastran method outlined in this report (section II.B). A simple flow chart describing the approach is provided in figure 9.

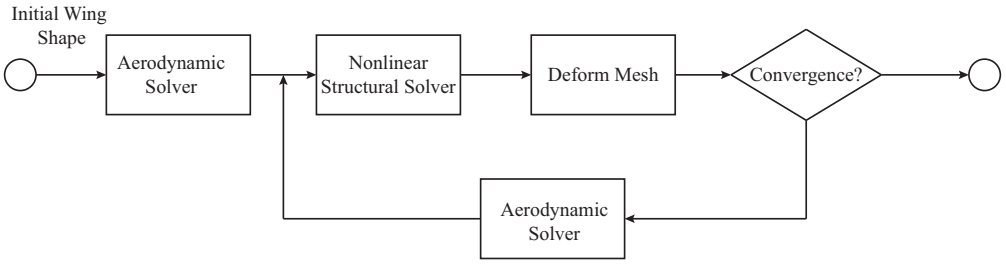


Figure 9: Convergence for NeoCASS aeroelastic solver

The aerodynamic solver (Strip theory or VLM) is performed on the undeformed rigid mesh to allow an initial load case for the nonlinear structural solver. The load is then applied incrementally. At each load step the stiffness matrix is recalculated which, combined with the internal forces, allow the recovery of displacements. Convergence, based on the change in displacements, terminates the structural loop. The mesh is deformed based on the structural displacements, obtained from the final load step, using an infinite plate spline method. The aerodynamic solver recalculates the forces which once again sets up the problem for the nonlinear structural solver. The iterative loop, coupling the aerodynamic and structural solver, terminates upon convergence based on displacements. Numerical damping is added to prevent any initial overshoot from the applied aerodynamic load.

## II.D. Intrinsic Beam Model

This section gives an overview of the methodologies used for carrying out static aeroelastic analysis using an intrinsic beam model. First, the PDEs that describe the beam dynamics are introduced and reduced to a static equation, then the finite-element discretization is described as one method for obtaining an approximate solution to the equations for the general case.

### *II.D.1. Beam Definitions and Kinematics*

It is first beneficial to formalise the definitions of the variables, labels and operators which will be used in this description as a basis for the remainder of the beam description.

First, the frames of reference of the problem are defined and labelled. A global/inertial frame is defined using the label **G**, and a body-fixed reference frame is denoted with the label **a**. An additional frame, **B**, is defined as the reference frame local to the deformed beam. Strip-theory aerodynamics make use of an

aerodynamic reference frame labelled **A**, which is defined as a frame aligned with the zero-lift angle of attack of a given aerofoil.

An additional frame is added which is aligned with the inflow velocity, providing a convenient frame in which to define lift and drag forces and to align the gravitational vectors to these forces. This frame is defined using the label **I**.

A 1-dimensional curvilinear reference frame is included into the beam description which gives the coordinate along the beam, and denoted by $s \in \mathbb{R}^1$.

With reference frames introduced, variables can be described, with sub- and superscripts used to denote the reference frame in which certain variable are defined. The position of a given point on the beam, in the body-fixed frame, **a**, can be given as the vector, $\boldsymbol{R}_a(s) \in \mathbb{R}^{3\times1}$. The rotation matrix between two reference frames is denoted $[C^{xy}(s)] \in \mathbb{R}^{3\times3}$ where $x$ and $y$ are any two reference frames.

Strains, $\boldsymbol{\gamma} \in \mathbb{R}^{3\times1}$, and curvatures, $\boldsymbol{\kappa} \in \mathbb{R}^{3\times1}$, will be used as degrees of freedom for this beam formulation, and are described as,[16]

$$\boldsymbol{\gamma}_B(s) = [C^{Ba}(s)]\boldsymbol{R}_a(s)' - \boldsymbol{e}_2 \tag{8}$$

and

$$\tilde{\boldsymbol{\kappa}}_B(s) = [C^{Ba}(s)][C^{aB}(s)]' \tag{9}$$

where $\bullet'$ denotes the spatial derivative with spanwise coordinate $s$, $\tilde{\bullet}$ is the cross-product matrix operator of a given variable, and $\boldsymbol{e}_2 := [0;1;0]$. The slight variation in the strain definition used in this work compared to the literature (Hodges[11] for example), should be noted, where typically the $\boldsymbol{e}_2$-vector used here is replaced with $\boldsymbol{e}_1 = [1;0;0]$. This minor change to the strain definition ensures that the coordinate system in this beam description is consistent with the other methods defined in this work.
The curvature vector, $\boldsymbol{\kappa}_B$, can also be written as.

$$\boldsymbol{\kappa}_B = \begin{Bmatrix} \kappa_x \\ \tau \\ \kappa_z \end{Bmatrix} \tag{10}$$

where $\tau$ is used to denote a torsional curvature.

### *II.D.2. Intrinsic Beam Equation*

In this work, an implementation of Hodges' intrinsic beam model will be formed for use in nonlinear analyses of aircraft structures. The following equations give the intrinsic beam equations in their strong form.[11]

$$[M]\begin{Bmatrix}\dot{\boldsymbol{V}}\\ \dot{\boldsymbol{\Omega}}\end{Bmatrix} + \begin{bmatrix}\tilde{\boldsymbol{\Omega}} & 0\\ \tilde{\boldsymbol{V}} & \tilde{\boldsymbol{\Omega}}\end{bmatrix}[M]\begin{Bmatrix}\boldsymbol{V}\\ \boldsymbol{\Omega}\end{Bmatrix} = \begin{Bmatrix}\boldsymbol{F}'\\ \boldsymbol{M}'\end{Bmatrix} - \begin{bmatrix}\tilde{\boldsymbol{F}} & 0\\ \tilde{\boldsymbol{M}} & \tilde{\boldsymbol{F}}\end{bmatrix}[C]\begin{Bmatrix}\boldsymbol{F}+\boldsymbol{e}_f\\ \boldsymbol{M}\end{Bmatrix} + \begin{Bmatrix}\boldsymbol{f}\\ \boldsymbol{m}\end{Bmatrix} \tag{11}$$

$$[C]\begin{Bmatrix}\dot{\boldsymbol{F}}\\ \dot{\boldsymbol{M}}\end{Bmatrix} = \begin{Bmatrix}\boldsymbol{V}'\\ \boldsymbol{\Omega}'\end{Bmatrix} - \begin{bmatrix}\tilde{\boldsymbol{\Omega}} & \tilde{\boldsymbol{V}}\\ 0 & \tilde{\boldsymbol{\Omega}}\end{bmatrix}[C]\begin{Bmatrix}\boldsymbol{F}+\boldsymbol{e}_f\\ \boldsymbol{M}\end{Bmatrix} \tag{12}$$

Here, $\boldsymbol{V}(s) \in \mathbb{R}^{3\times1}$ and $\boldsymbol{\Omega}(s) \in \mathbb{R}^{3\times1}$ refer to linear and rotational velocities in the local beam axes, and $\boldsymbol{F}(s) \in \mathbb{R}^{3\times1}$ and $\boldsymbol{M}(s) \in \mathbb{R}^{3\times1}$ refer to the local internal force and moments along the beam. External forces and moments are applied to the system through the $\boldsymbol{f}(s) \in \mathbb{R}^{3\times1}$ and $\boldsymbol{m}(s) \in \mathbb{R}^{3\times1}$ vectors.

The subscript **B** is dropped from these variable labels, along with explicit mention that they are functions of beam coordinate, $s$, for clarity since all variables are in the local frame and any variable or beam property can in general vary along the beam. The $\dot{\bullet}$ operator represents the temporal derivatives of a certain

variable. Finally, the matrices $[M(s)] \in \mathbb{R}^{6\times6}$ and $[C(s)] \in \mathbb{R}^{6\times6}$ are the mass and compliance matrices, respectively, and are given as

$$\begin{Bmatrix} \boldsymbol{P} \\ \boldsymbol{H} \end{Bmatrix} = [M] \begin{Bmatrix} \boldsymbol{V} \\ \boldsymbol{\Omega} \end{Bmatrix} = \begin{bmatrix} m & -m\tilde{\boldsymbol{\xi}}_{cg} \\ m\tilde{\boldsymbol{\xi}}_{cg} & J \end{bmatrix} \begin{Bmatrix} \boldsymbol{V} \\ \boldsymbol{\Omega} \end{Bmatrix} \tag{13}$$

and

$$\begin{Bmatrix} \boldsymbol{\gamma} \\ \boldsymbol{\kappa} \end{Bmatrix} = [C] \begin{Bmatrix} \boldsymbol{F} \\ \boldsymbol{M} \end{Bmatrix} = \begin{bmatrix} c_{\gamma f} & c_{\gamma m} \\ c_{\kappa f} & c_{\kappa m} \end{bmatrix} \begin{Bmatrix} \boldsymbol{F} \\ \boldsymbol{M} \end{Bmatrix} \tag{14}$$

which relate velocities to momenta, and forces and moments to strains and curvatures. Here $P$ and $H$ are linear and angular momenta respectively. The final value to define is $\boldsymbol{e}_f = c_{\gamma f}\boldsymbol{e}_1$.

For this work, static aeroelastic analyses are considered only, and as such, any time derivatives and velocity terms can be removed from equations (11) and (12) to arrive at the static equations. Equation (12) disappears entirely, and equation (11) reduces down to

$$\begin{bmatrix} \tilde{\boldsymbol{F}} & 0 \\ \tilde{\boldsymbol{M}} & \tilde{\boldsymbol{F}} \end{bmatrix} [C] \begin{Bmatrix} \boldsymbol{F} + \boldsymbol{e}_f \\ \boldsymbol{M} \end{Bmatrix} - \begin{Bmatrix} \boldsymbol{F}' \\ \boldsymbol{M}' \end{Bmatrix} = \begin{Bmatrix} \boldsymbol{f} \\ \boldsymbol{m} \end{Bmatrix} \tag{15}$$

*II.D.3. Finite-element approach*

In order to solve the general PDEs in equations (11) and (12), a finite-element approach is used. In order to carry this out, the strong form of the equations must be transformed into the weak form for formulating the finite-element matrices, as described in Ref.[16] These can be written as

$$\int_{t_1}^{t_2} \int_0^l \begin{Bmatrix} \delta\boldsymbol{R} \\ \delta\boldsymbol{\Phi} \end{Bmatrix}^T \left( - \begin{Bmatrix} \boldsymbol{F}' \\ \boldsymbol{M}' \end{Bmatrix} + \begin{bmatrix} \tilde{\boldsymbol{F}} & 0 \\ \tilde{\boldsymbol{M}} & \tilde{\boldsymbol{F}} \end{bmatrix} [C] \begin{Bmatrix} \boldsymbol{F} + \boldsymbol{e}_f \\ \boldsymbol{M} \end{Bmatrix} - \begin{Bmatrix} \boldsymbol{f} \\ \boldsymbol{m} \end{Bmatrix} \right) \mathrm{d}s \, \mathrm{d}t = \boldsymbol{0} \tag{16}$$

where $\delta\boldsymbol{R}$ and $\delta\boldsymbol{\Phi}$ are incremental linear and rotational displacements, respectively. Using the weak form of these equations, a finite-element approach can be applied. In this work, linear finite elements are used for the virtual values, as in Ref.[13] In this scheme, it is assumed that the elemental values vary linearly with $s$, but due to the weak form FEM approach only solving for element average values (the integral of the PDE is solved for), a constant value for each element is obtained. Under the assumptions of linear distributions, nodal values can be obtained from the elemental average values given some boundary condition. Furthermore, it is assumed that stiffness and mass properties are constant along each element, but free to vary from element to element down the beam length.

Therefore, it can be written that,

$$\begin{Bmatrix} \delta\boldsymbol{R}(s) \\ \delta\boldsymbol{\Phi}(s) \end{Bmatrix} = [A_1 + A_2 s] \begin{Bmatrix} \delta\boldsymbol{R}_n \\ \delta\boldsymbol{\Phi}_n \\ \delta\boldsymbol{R}_{n+1} \\ \delta\boldsymbol{\Phi}_{n+1} \end{Bmatrix} \tag{17}$$

valid only over a distance on the beam from $s_n$ to $s_{n+1} = s_n + \Delta s$, where $\Delta s$ is the element length, and the matrices $[A_1] \in \mathbb{R}^{6\times12}$ and $[A_2] \in \mathbb{R}^{6\times12}$ are constant, given as

$$[A_1] = \begin{bmatrix} I_{6\times6} & 0_{6\times6} \end{bmatrix} \tag{18}$$

and

$$[A_2] = \frac{\begin{bmatrix} -I_{6\times6} & I_{6\times6} \end{bmatrix}}{\Delta s} \tag{19}$$

.

The beam equations can now be written in a concise manner,

$$[K(\boldsymbol{X})]\,\boldsymbol{X} - \boldsymbol{f} = \boldsymbol{0} \tag{20}$$

where $[K]$ is the system stiffness matrix, which can be obtained using the linear approximations defined earlier, and $\boldsymbol{X}$ is a vector of elemental beam forces and moments. The elemental system matrix $[K]_e$ can be written as

$$\begin{aligned}[K]_e &= \left[A_1^T \Delta s + A_2^T \frac{\Delta s^2}{2}\right]_e \begin{bmatrix} \tilde{\boldsymbol{\kappa}} & 0_{3\times 3} \\ \tilde{\boldsymbol{\gamma}} + \tilde{\boldsymbol{e}}_1 & \tilde{\boldsymbol{\kappa}} \end{bmatrix}_e + \left[A_2^T \Delta s\right]_e \\ &= \begin{bmatrix} K_{e1} \\ K_{e1} \end{bmatrix}\end{aligned}$$

using integration by parts on the spatial derivatives of $\mathbf{F}$ and $\mathbf{M}$. The total stiffness matrix and state vectors can be then written as

$$[K] = \begin{bmatrix} K_{11} & 0 & 0 & \dots & 0 \\ K_{12} & K_{21} & 0 & \dots & 0 \\ 0 & K_{22} & K_{31} & \dots & 0 \\ \vdots & \vdots & \vdots & \ddots & 0 \\ 0 & 0 & 0 & K_{(n-1)2} & K_{n1} \\ 0 & 0 & 0 & 0 & K_{n2} \end{bmatrix} \in \mathbb{R}^{(6n+1)\times 6n}, \boldsymbol{X} = \begin{Bmatrix} \boldsymbol{F}_1 \\ \boldsymbol{M}_1 \\ \boldsymbol{F}_2 \\ \boldsymbol{M}_2 \\ \vdots \\ \boldsymbol{F}_n \\ \boldsymbol{M}_n \end{Bmatrix} \in \mathbb{R}^{6n\times 1} \tag{21}$$

for $n$ elements. The first six rows of the stiffness matrix, $[K]$, can be removed to provide a $6n \times 6n$ matrix to model a cantilevered beam.

### *II.D.4. Obtaining beam displacements and orientations*

As the beam dynamical equations used in this work solve directly for internal beam loads, the displacements and orientations of points on the beam are not explicitly available from the system states. In order to obtain the global beam properties, additional equations are required. There are two different approaches to this problem; one is free to choose an integration of the local velocities with respect to time, or the strains and curvatures with respect to beam coordinate in order to calculate beam positions and orientations. For the static problem, the latter approach will be used.

#### Spatial Integration of Strains and Curvatures

The spatial integration of the strains and curvatures can be achieved using the definitions of strains and curvatures given earlier in equations (8) and (9). These can be rearranged to give the spatial derivatives of the location and orientations in terms of strains and curvatures, such that

$$\boldsymbol{R}_a'(s) = \left[C^{aB}(s)\right](\boldsymbol{\gamma}_B(s) + \boldsymbol{e}_1) \tag{22}$$

and

$$\left[C^{aB}(s)\right]' = \left[C^{aB}(s)\right]\tilde{\boldsymbol{\kappa}}_B(s) \tag{23}$$

or, combined into one equation,

$$\begin{bmatrix}\boldsymbol{R}_a(s) & C^{aB}(s)\end{bmatrix}' = \left[C^{aB}(s)\right]\begin{bmatrix}\boldsymbol{\gamma}_B(s) + \boldsymbol{e}_1 & \tilde{\boldsymbol{\kappa}}_B(s)\end{bmatrix} \in \mathbb{R}^{3\times 4} \tag{24}$$

This equation can be solved easily providing an element of constant strain and curvature is used by using the usual matrix exponential solution. The position and orientation of a beam can then be written as

$$\begin{bmatrix}\boldsymbol{R}_a(s) & C^{aB}(s)\end{bmatrix} = \left[C_0^{aB}\right] e^{\begin{bmatrix}\boldsymbol{\gamma}_{B_e} + \boldsymbol{e}_1 & \tilde{\boldsymbol{\kappa}}_{B_e}\end{bmatrix}(s-s_0)} \tag{25}$$

valid only for element, $e$. The position and orientation of some node $s_{n+1}$ can be known from the position and orientation of the previous node $s_n$, along with the strain and curvature of the element which joins them, such that

$$\begin{bmatrix} \boldsymbol{R_a}(s_{n+1}) & C^{aB}(s_{n+1}) \end{bmatrix} = \begin{bmatrix} C^{aB}(s_n) \end{bmatrix} e^{\begin{bmatrix} \boldsymbol{\gamma}_{B_e} + \boldsymbol{e}_1 & \tilde{\boldsymbol{\kappa}}_{B_e} \end{bmatrix} \Delta s} \tag{26}$$

Furthermore, any intermediate point on the element can be determined using this relationship, allowing an arbitrary number of location points to be retrieved from a single element.

### II.E. Continuous shape function reduced order model

The reduced order modelling approach is based around the expression of the wing deflection as a weighted sum of shape profiles. This is not entirely dissimilar to how one would express a flexible structure as a linear summation of modes. The advantages of such a characterisation lie in the potential reduction of model complexity and resultant run time, thus allowing for the rapid assessment of multiple test cases in quick succession. Furthermore, such low order descriptions facilitate the further application of more specialised nonlinear analysis techniques which can help to identify different possible system behaviours without a strong reliance on costly Monte-Carlo type search strategies.

A key disadvantage of more traditional modal decomposition techniques, however, lies in their inability to capture key geometric nonlinearities stemming from highly deflected configurations; for example, 'tip shortening' type effects. This is mitigated by the model reduction strategy presented here by employing shape profiles describing the orientation of a local reference frame that remains aligned with the wing as it deflects. Figure 10 illustrates this concept showing an example deflected wing profile. $\Gamma$ is used to denote the position vector of the beam axis (mid-chord in this paper) - defined from an arbitrary point $O$ - parametrised by the span-wise coordinate $s$. For the example $\Gamma(s)$ shown in the figure a local set of coordinate axis $(\mathbf{e}_x, \mathbf{e}_y, \mathbf{e}_z)$ is depicted such that $\mathbf{e}_y$ is in the local span-wise direction, $\mathbf{e}_z$ normal to wing surface and $\mathbf{e}_x$ in the chord-wise direction. By specifying the variation in the orientation of $\mathbf{e}_x, \mathbf{e}_y, \mathbf{e}_z$ with respect to $s$ one uniquely defines the wing shape in 3D space.

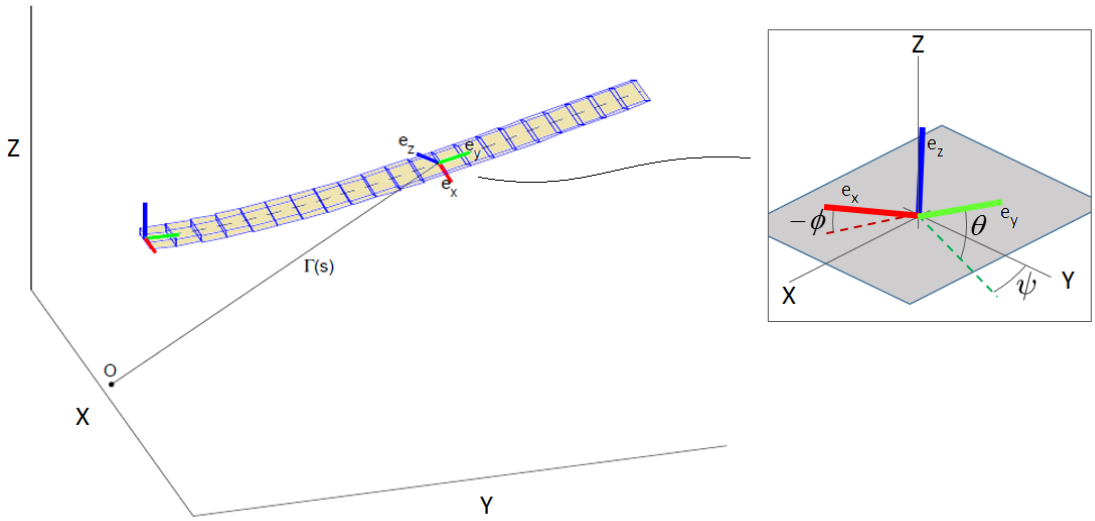


Figure 10: Geometric representation of a flexible structure. The 3D profile is uniquely determined by the span-wise variation of the local coordinate frame $(\mathbf{e}_x, \mathbf{e}_y, \mathbf{e}_z)$.

Representation of the local coordinate orientation is accomplished using a system of Euler angles $(\theta, \phi, \psi)$

shown in the inset box of figure 10. Using these angles, the orientation of the local coordinate axis vectors in the global coordinate system may be written:

$$\begin{pmatrix}\mathbf{e}_x\\ \mathbf{e}_y\\ \mathbf{e}_z\end{pmatrix} = \begin{pmatrix}\cos\psi\cos\phi + \sin\theta\sin\psi\sin\phi & -\sin\psi\cos\phi + \sin\theta\cos\psi\sin\phi & \cos\theta\sin\phi\\ \cos\theta\sin\psi & \cos\theta\cos\psi & \sin\theta\\ \cos\psi\sin\phi - \sin\theta\sin\psi\cos\phi & -\sin\psi\sin\phi - \sin\theta\cos\psi\cos\phi & \cos\theta\cos\phi\end{pmatrix} \quad . \tag{27}$$

What follows is a derivation of the governing static equations modelling the 1D beam representation of a wing. Firstly, the stiffness potential function is introduced capturing the strain energy of the deflected structure. The effects of external forces exerted on the wing are then incorporated via the treatment of additional virtual work terms.

### *II.E.1. Stiffness Potential*

Modelling the wing as a 1D long slender beam with negligible shear effects, one may relate the energy potential of the deflected wing to the local curvature along its axis. This yields the net potential energy integrated along the beam as

$$V = \int_0^L \int M_{EIxx}(\kappa_x)\,\mathrm{d}\kappa_x\,\mathrm{d}s + \int_0^L \int M_{EIzz}(\kappa_z)\,\mathrm{d}\kappa_z\,\mathrm{d}s + \int_0^L \int M_{GJ}(\tau)\,\mathrm{d}\tau\,\mathrm{d}s \quad , \tag{28}$$

where L is the total length of the beam and $M_{EIxx}(\kappa_x), M_{EIzz}(\kappa_z), M_{GJ}(\tau)$ are generic nonlinear moment-curvature relationships. For this study these are given the linear form:

$$\begin{aligned} M_{EIxx}(\kappa_x) &= EI_{xx}\kappa_x\\ M_{EIzz}(\kappa_z) &= EI_{zz}\kappa_z\\ M_{GJ}(\tau) &= GJ\tau \end{aligned} \tag{29}$$

where $E$ is the material Young's modulus, $G$ the shear modulus, $I_{xx}$ and $I_{zz}$ are 2nd moments of area about the local $\mathbf{e}_x$ and $\mathbf{e}_z$ axis respectively and $J$ is the sectional torsion constant.

Curvature of the beam is expressed by $\kappa_x$ and $\kappa_z$ (again about $\mathbf{e}_x$ and $\mathbf{e}_z$) and $\tau$ gives the twist per unit length. These curvatures and twists relate to the spanwise variation of the local coordinate vectors $(\mathbf{e}_x, \mathbf{e}_y, \mathbf{e}_z)$ such that

$$\begin{pmatrix}\mathbf{e}'_x\\ \mathbf{e}'_y\\ \mathbf{e}'_z\end{pmatrix} = \begin{pmatrix}0 & -\kappa_z & \tau\\ \kappa_z & 0 & \kappa_x\\ -\tau & -\kappa_x & 0\end{pmatrix}\begin{pmatrix}\mathbf{e}_x\\ \mathbf{e}_y\\ \mathbf{e}_z\end{pmatrix} \quad , \tag{30}$$

where $*'$ denotes the spanwise derivative (i.e. with respect to $s$).

Based on equations (30) and (27) $\kappa_x$, $\kappa_z$ and $\tau$ may be written:

$$\begin{aligned} \kappa_x &= \mathbf{e}'_y\cdot\mathbf{e}_z = -\mathbf{e}'_z\cdot\mathbf{e}_y\\ \kappa_z &= \mathbf{e}'_y\cdot\mathbf{e}_x = -\mathbf{e}'_x\cdot\mathbf{e}_y\\ \tau &= \mathbf{e}'_z\cdot\mathbf{e}_x = -\mathbf{e}'_x\cdot\mathbf{e}_z \end{aligned} \quad \Longrightarrow \quad \begin{aligned} \kappa_x &= \psi'\cos\theta\sin\phi + \theta'\cos\phi\\ \kappa_z &= \psi'\cos\theta\cos\phi - \theta'\sin\phi\\ \tau &= \phi' - \psi'\sin\theta \quad . \end{aligned} \tag{31}$$

### *II.E.2. Virtual Work terms*

Additional forces acting on the system are incorporated based on the concept of virtual work. These forces consist of self weight as well as the aerodynamic loads generated by the aerofoil geometry. In general for an

example force vector $P$ applied at position $r$ the virtual work is given by

$$\delta W_P = \int_0^L \mathbf{P}(s) \cdot \delta \mathbf{r} \, \mathrm{d}s \quad . \tag{32}$$

Here the point of force application $r$ is given the form $r = \Gamma + a\mathbf{e}_x + c\mathbf{e}_z$ where $\Gamma$ is obtained via spanwise integration of $\mathbf{e}_y$. The vectors $\mathbf{e}_x$ and $\mathbf{e}_z$ take the point of application away from the beam centreline.

Similarly for an applied moment vector $M$ applied over the incremental rotation $\delta\xi$ the work done is

$$\delta W_M = \int_0^L \mathbf{M}(s) \cdot \delta \xi \, \mathrm{d}s \quad , \tag{33}$$

with the incremental rotation related to the Euler angles $(\theta, \psi, \phi)$ such that

$$\delta\xi = \delta\theta \, (\cos\psi, -\sin\psi, 0) + \delta\psi \, (0, 0, -1) + \delta\phi \, \mathbf{e}_y \quad .$$

For this study these forces result from the effect of self weight as well as the aerodynamic loads generated by the aerofoil geometry. Modelling of these aerodynamic loads is achieved via the steady vortex lattice treatment discussed in section II.G.1.

The describing set of static equations for this system is obtained by equating incremental variations in the strain energy to the work done on the system. These variations are considered with respect to the generalised coordinates $\mathbf{q}$ which approximate the deflected profile of the beam. This relation may be written as:

$$-\frac{\partial V}{\partial q_i} = \frac{\partial \delta W}{\partial q_i} \tag{34}$$

The choice of generalised coordinates $q$ here relate to a finite set of characterising shape functions onto which the continuous problem is projected. Specifically the Euler angles describing the variation in the local coordinate system $(\mathbf{e}_x, \mathbf{e}_y, \mathbf{e}_z)$ are expressed as a linear summation of shapes which, when given a form separable in the spanwise coordinate $(s)$ and time $(t)$, may be written:

$$\theta(s,t) = \sum_{i=1}^{n} \Theta_i(s) q_i(t) \, , \qquad \psi(s,t) = \sum_{j=1}^{m} \Psi_j(s) p_j(t) \, , \qquad \phi(s,t) = \sum_{k=1}^{r} \Phi_k(s) r_k(t) \tag{35}$$

$\Theta, \Psi, \Phi$ are the sets of spatial shape functions corresponding to each Euler angle with $q(t), p(t), r(t)$ their time dependent weightings. The number of shape functions utilized may be assigned based on the desired speed or accuracy of the solution sought. The efficiency of convergence as more functions are added may also be influenced by the specific shape-profiles used (linearised mode shapes, static trim shapes, etc.). This choice can have a significant effect on the efficiency of convergence for a given number of shape functions.[20]

The static equations follow from evaluation of equation (34) with constituent terms given by equations (28), (32) and (33). This yields the system:

$$\int_0^L EI_1 \, \kappa_z \frac{\partial \kappa_z}{\partial q_i} + EI_2 \, \kappa_x \frac{\partial \kappa_x}{\partial q_i} + GJ \, \tau \frac{\partial \tau}{\partial q_i} \, \mathrm{d}\tilde{s} = \int_0^L \mathbf{P}(\tilde{s}) \cdot \frac{\partial \mathbf{r}}{\partial q_i} + \mathbf{M}(\tilde{s}) \cdot \frac{\partial \xi}{\partial q_i} \, \mathrm{d}\tilde{s} \quad . \tag{36}$$

For this study six polynomial shape functions are chosen to represent the spanwise distribution of each of the three characterising Euler angles (fig. 10). These shapes are depicted in figure 11 and are integrated to form $\theta(s)$, $\psi(s)$ and $\phi(s)$ such that they each satisfy the kinematic boundary conditions of zero root twist, dihedral and sweep. Although not essential, the natural boundary conditions of zero tip-moment and tip-shear (for the aeroelastic case) are also satisfied by considering shape-sets progressing from starting polynomials of 2nd or 3rd orders respectively. This yields a static system comprising 18 equations from which the results of this study are generated.

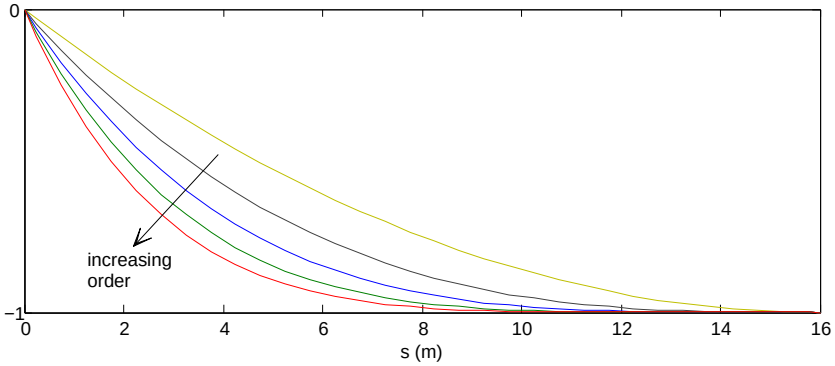


Figure 11: Polynomial basis set used to approximate the spanwise derivatives of the Euler angles $\theta$, $\psi$ and $\phi$. These shape functions are shown in increasing order as indicated by the arrow.

#### *II.E.3. Aerodynamic Forces*

Aerodynamic forces enter the system as components of the applied force and moment distributions, $P$ and $M$ respectively. These forces are calculated based on a standard steady vortex lattice implementation. This aerodynamic formulation is also shared by the intrinsic beam (§II.D) and rigid multibody (§II.F) dynamic methods and is discussed in more detail in section II.G.

### II.F. Rigid Element Multi-Body Dynamics

Multibody dynamics simulation[19] is a convenient tool capable of simulating multiphysics systems with arbitrary types of nonlinearities and both rigid and flexible components. In the fixed-wing aeroelasticity field, it has been employed for the trim and simulation of manoeuvring flexible aircraft coupled with aerodynamic methods of various levels of fidelity.[7,15]

For the nonlinear aeroelasticity of very flexible aircraft, there have been applications of multibody simulation by Krüger et al[14] and Zhao et al,[22] respectively for the study of the flight mechanics stability of a HALE configuration and for the aeroelastic stability analysis and flight control in manoeuvres of a UAV-like flexible aircraft. Since multibody dynamics allows for arbitrary large displacements and rotations, its distinct advantage for these types of configurations is the intrinsic and straightforward capability to take into account the interactions between rigid body modes, linked to flight mechanics, and aeroelasticity, without the need for dedicated formulations. The multibody software employed for this work is LMS Virtual.Lab Motion v.13.1.[2]

In the following the equations of motion of a multibody system are briefly outlined. Each body is described by a set of Cartesian coordinates, identifying the location of its centre of gravity in the global reference frame. The vector of the generalized coordinates of the i-th body is thus

$$\mathbf{q}_i = \{x, y, z, e_0, e_1, e_2, e_3\}$$

where $x, y, z$ are the Cartesian coordinates and $e_0, e_1, e_2, e_3$ the (redundant) quaternion parameters used to describe the orientation of the body and to avoid singularity occurring with other representations, e.g. Euler angles.

The bodies in the system are connected together by joints and kinematic relationships, which are expressed as general nonlinear algebraic constraint equations

$$C(\mathbf{q}, \dot{\mathbf{q}}, t) = 0$$

Differentiating these equations twice with respect to time $t$, one obtains the kinematic acceleration equations

$$\mathbf{C_q}\ddot{\mathbf{q}} = \mathbf{Q_d}$$

where

$$\mathbf{Q_d} = -\mathbf{C_t t} - (\mathbf{C_q}\dot{\mathbf{q}})_\mathbf{q}\dot{\mathbf{q}} - 2\mathbf{C_{qt}}\dot{\mathbf{q}} \quad .$$

Subscripts $*_q$ and $*_t$ denote partial differentiation with respect to the indicated variable. The dynamic equations of motion, e.g. derived from Lagrange method, are, for the i-th body,

$$\mathbf{M}_i\ddot{\mathbf{q}}_i + \mathbf{C}_{q,i}^T\lambda_i = \mathbf{Q}_{e,i} + \mathbf{Q}_{v,i}$$

with $\mathbf{M}_i$ mass matrix, $\lambda_i$ vector of Lagrange multipliers, $\mathbf{Q}_{e,i}$ vector of generalized applied forces and $\mathbf{Q}_{v,i}$ vector of velocity dependent terms. Adding the kinematic relationships to the equations of motion, a system of nonlinear Differential Algebraic Equations (DAE) describing the kinematics and dynamics of a multibody system is obtained;

$$\begin{pmatrix} \mathbf{M} & \mathbf{C}_q^T \\ \mathbf{C}_q & \mathbf{0} \end{pmatrix} \begin{pmatrix} \ddot{\mathbf{q}} \\ \lambda \end{pmatrix} = \begin{pmatrix} \mathbf{Q}_e + \mathbf{Q}_v \\ \mathbf{Q}_d \end{pmatrix} \quad .$$

The equations are nonlinear, the matrices being functions of the vector of generalized coordinates itself, and are solved by a Backward Differentiation Formula (BDF) integrator.[9]

The bodies can be considered either as rigid or flexible. The most common approach to model flexibility is a modal representation based on Component Mode Synthesis from FEM,[5] which adds to the generalized coordinates the modal participation factors of each mode used to represent a body's flexibility. This however limits the applicability to linear structures with small elastic displacements. Formulations based on nonlinear FE beams[10] and generic nonlinear FEM elements[4] have also been proposed for this purpose.

The work presented in this paper employs a simpler yet efficient approach to model a flexible wing with arbitrary large elastic displacements. It is based on the discretization of the wing by a series of rigid bodies, to which inertial properties are assigned, interconnected by beam force elements, representing the stiffness distribution. These beam element can be interpreted as a general 6DOF spring which may have cross-couplings in the K matrix. In the literature this modelling technique has been known as the Finite Segment approach[8] and it has been successfully used for the study of very flexible aircraft.[14,22] Since the multibody formulation allows arbitrarily large rigid body motion, each wing section can undergo large displacements and rotations and the ensuing internal forces are determined based on this displacement field. Each multibody beam element connects two consecutive rigid bodies and has a stiffness matrix derived from FE linear 6DOF beam theory and the usual cross-sectional properties ($EA$, $EI$, $GJ$) are assigned to it. The relative forces and moments $\mathbf{F}_{el}$ exchanged between the two connected bodies are calculated as

$$\mathbf{F}_{el} = \mathbf{K}\mathbf{x} + \mathbf{D}\dot{\mathbf{x}}$$

where $\mathbf{x}$ and $\dot{\mathbf{x}}$ are the relative displacements and velocities; $\mathbf{K}$ and $\mathbf{D}$ are the linear stiffness and damping matrices. The stiffness matrix is a 6x6 symmetric matrix given by

$$\mathbf{K} = \begin{bmatrix} \frac{EA}{l} & 0 & 0 & 0 & 0 & 0 \\ 0 & \frac{12EI_z}{l^3} & 0 & 0 & 0 & -\frac{6EI_z}{l^2} \\ 0 & 0 & \frac{12EI_y}{l^3} & 0 & -\frac{6EI_y}{l^2} & 0 \\ 0 & 0 & 0 & \frac{GI_x}{l} & 0 & 0 \\ 0 & 0 & -\frac{6EI_z}{l^2} & 0 & \frac{4EI_y}{l} & 0 \\ 0 & \frac{6EI_y}{l^2} & 0 & 0 & 0 & \frac{4EI_z}{l} \end{bmatrix} \quad .$$

The damping is proportional to the diagonal of the stiffness matrix by a damping factor $\xi$, i.e.

$$\mathbf{D} = \xi \cdot diag(\mathbf{K}) \quad .$$

The aerodynamic model is based on strip theory. Though more simplistic than higher-fidelity methods, this approach is suitable and still accurate for high aspect ratio wings. To further support this choice, strip theory can be straightforwardly integrated with the wing Finite Segment representation because no interpolation process is required between the aerodynamic and structural meshes: the aerodynamic forces and moments are applied at the aerodynamic centre of each rigid body, which represents a strip. Further details of the aerodynamic implementation are covered in section II.G.

### II.G. Aerodynamic Modelling

In addition to the structural models introduced so far in section II, a suitable representation of static aerodynamic loads is required to close the aeroelastic formulations. In this paper, the aim is to keep the aerodynamic descriptions as consistent as possible between the different approaches. As such, the continuous-shape-function, intrinsic beam method and NeoCASS approaches all employ an uncorrected vortex-lattice method (VLM) to provide the aerodynamic loads. The iterative Nastran approach varies slightly by using Nastran's in-built doublet-lattice method (DLM), which for the static case will tend towards the VLM formulation using a small angle approximation. The multibody rigid element formulation is restricted to a strip theory aerodynamics description, but makes use of the DLM aero loads solved for the undeformed rigid case to obtain a spanwise lift distribution and account in part for the 3D tip loss effects.

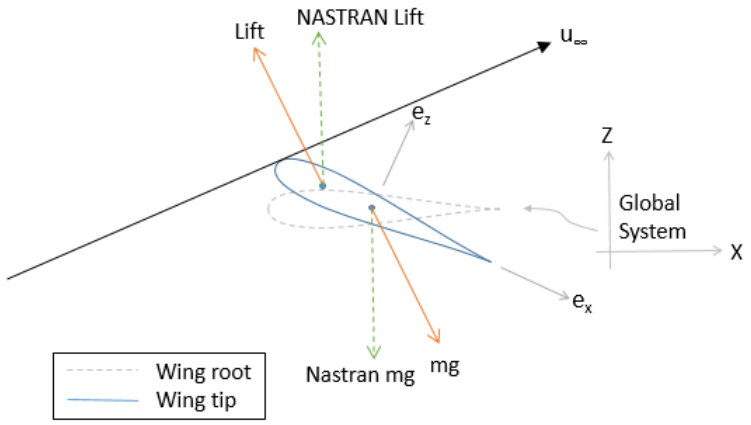


Figure 12: The global coordinate system in which aerodynamic and structural displacements are defined. The orientation of lift and gravitational vectors treated by the aeroelastic models are also indicated.

In order to examine specific implementations of these methods, some coordinate systems must be defined for clarification. These coordinate systems are illustrated in figure 12. The orientation of the global coordinate system is illustrated and defined such that the $X$-axis (with direction vector $\boldsymbol{e}_X$) is aligned along the root chord direction; the $Z$-axis, $\boldsymbol{e}_Z$, is normal to the root chord direction, i.e. perpendicular to $\boldsymbol{e}_X$ with no spanwise component; the global $Y$-axis, $\boldsymbol{e}_Y$, is the cross-product of $\boldsymbol{e}_X$ and $\boldsymbol{e}_Z$, and extends spanwise down the undeformed wing (assuming a wing free of sweep and dihedral), completing the orthogonal $(X, Y, Z)$ global coordinate system. A local beam coordinate system, $(x, y, z)$ is also defined along the length of the beam, $s$, where the $x$-axis, $\boldsymbol{e}_x(s)$, is parallel to the zero-lift angle of attack at a given beam location, the $y$-axis, $\boldsymbol{e}_y(s)$, is parallel to the local beam coordinate, and the $z$-vector, $\boldsymbol{e}_z(s)$, is normal to both these vectors (see also figure 10 for reference). The global and local coordinate frames coincide for the undeformed case,

and at all times at the root ($(\boldsymbol{e}_x(0), \boldsymbol{e}_y(0), \boldsymbol{e}_z(0)) = (\boldsymbol{e}_X, \boldsymbol{e}_Y, \boldsymbol{e}_Z)$). A rotation matrix from the global to the local frames can be defined as,

$$\left[C^{GB}(s)\right] = [\boldsymbol{e}_x(s), \boldsymbol{e}_y(s), \boldsymbol{e}_z(s)] \tag{37}$$

The free stream flow vector is defined in this system by a rotation in the global frame. For a simple angle of attack case as considered in this work, the flow vector becomes a rotation about the global $Y$-axis. Therefore, the inflow velocity vector can be determined as

$$\boldsymbol{U}_G = \left[C^{GI}(\alpha)\right] \begin{bmatrix} 1 \\ 0 \\ 0 \end{bmatrix} U_\infty = \begin{bmatrix} \cos(\alpha) \\ 0 \\ \sin(\alpha) \end{bmatrix} U_\infty \tag{38}$$

for a given angle of attack $\alpha$.

Lift is defined perpendicular to the flow direction and local spanwise direction. The gravity vector is also aligned both perpendicular to the flow vector and to the global Y direction, such that,

$$m\boldsymbol{g}_I = m \begin{bmatrix} 0 \\ 0 \\ -g \end{bmatrix} \tag{39}$$

$$\boldsymbol{g}_G = \left[C^{GI}\right] \boldsymbol{g}_I = \begin{bmatrix} g\sin(\alpha) \\ 0 \\ -g\cos(\alpha) \end{bmatrix} \tag{40}$$

in the global frame of reference, where $g = 9.807 ms^{-1}$ is the acceleration due to gravity.

### *II.G.1. Vortex lattice code*

The VLM code generates a vortex circulation distribution, $\boldsymbol{\Gamma}(s)$. Vortices are aligned as horseshoe elements along the quarter chord line and trail off in the X direction; resultant forces are normal to the flow and local span vector $\boldsymbol{e}_y(s)$). The vortex circulation strength can be related to a generated force in the inflow frame by the Kutta-Joukowski theorem, such that

$$\boldsymbol{F}_I(s) = \rho U_\infty \boldsymbol{\Gamma}(s) \tag{41}$$

so that the $z$-component of $\boldsymbol{F}_I$ would be defined as the local lift force. Vortices are shed in the global $X$-direction, $\boldsymbol{e}_X$. No induced drag effects are included in this formulation, in order to aid agreement between the different methods.

The rigid multibody element and Nastran approaches vary from the VLM approach described so far, and will be discussed in detail next.

### *II.G.2. Rigid Multibody Element Strip Theory*

The LMS Virtual.Lab Motion software is restricted to a strip theory implementation only, and as such the aerodynamics description for this approach is necessarily different from the VLM methods already described. This method assumes that the lift generated at each spanwise strip is dependent only on the local angle of attack at that strip position, and is completely independent of lift generated at other points on the wing. For a given point on the wing, the local alpha, $\alpha_B$, can be calculated as

$$\alpha_B(s) = \sin^{-1}\left(\frac{\boldsymbol{e}_z(s).\boldsymbol{U}_G}{||\boldsymbol{U}_G||}\right) \tag{42}$$

and the lift per unit span can be determined at a given point on the wing as

$$L(s) = \frac{1}{2}\rho U_\infty c C_{L,\alpha}(s)\alpha_B(s) \tag{43}$$

where $c$ is the chord length, and $C_{L,\alpha}$ is the lift slope at a given span. The lift, $L$, acts normal to the local spanwise vector and the velocity vector. For 2D applications we can assume a lift slope of $2\pi$, but in this work the lift slope will be obtained from a DLM undeformed, rigid case, in order to match the DLM and VLM approaches more realistically.

#### *II.G.3. Nastran DLM*

The Nastran aerodynamics implementation is based on the standard in-built doublet-lattice method formulation used in static aeroelastic analyses. The classic approach to DLM aerodynamics is well documented[12] and will not be discussed in detail here.

For the static problem, the DLM method approaches that of the VLM providing a small angle approximation is applied to the VLM. However, the geometric application of forces from the DLM in Nastran differs from that in the VLM. For example, the linear assumption on the free stream vector places it in the global $X$-direction (aligned with $\boldsymbol{e}_X$) for any inflow angle of attack, rather than that aligned with the flow frame. Furthermore, the generated aerodynamic forces are applied normal to the undeformed structure, and so do not account for a change in spanwise orientation under large deformations (see figure 12). The iterative approach described here compensates for the latter limitations of the traditional Nastran implementation by aligning the aerodynamic panels to the deformed geometry, thus providing the nonlinear in-board component of the lift. However, the current implementation still applies the aerodynamic forces in the $YZ$-plane, neglecting any $x$-components. Additional differences observed between the DLM and VLM implementations are the linear assumption of through-flow at the 3/4 chord point (i.e. DLM through-flow approximated as $V\alpha$ rather than $V\sin\alpha$)), and the gravitational vector which is aligned in the global $-Z$ direction rather than perpendicular to the flow vector.

In order to demonstrate that any differences observed between the iterative Nastran method and the VLM methods are due to the remaining linear approximations that are not currently accounted for in the Nastran implementation, the NeoCASS aerodynamic code is also formulated such that it incorporates the aforementioned assumptions of the Nastran method. Results of the adapted NeoCASS code are also shown along with the original methodology to demonstrate the differences, and allows one to compensate for these differences when comparing Nastran to other results. It should be noted that the remaining linear assumptions in the iterative Nastran method could potentially be removed in further developments of the formulation.

## III. Comparative Results

The following sections detail a series of static solutions for the five different structural/aeroelastic methods introduced in section II. Initial tests comprise static tip load cases to demonstrate the ability of the structural models to capture geometric nonlinearities. After this, static aeroelastic analyses are carried out for various fixed angles of attack to investigate differences in the aerodynamics and structural couplings. Following this a number of aeroelastic quantities of interest are tracked as the root angle of attack is varied the results of which are compared with corresponding linear trends.

### III.A. Tip Load Comparison

First, the structural models are subjected to four tip load cases in order to validate the structural descriptions used in this work. The cases that are considered are 100N and 200N tip loads, applied as both global forces (vertical in the global frame) and follower forces (vertical in the beam local frame at the beam tip). The latter case models a force that remain orthogonal to the beam tangent line, and thus illustrates the ability of the modelling methods to correctly update the direction of this force as the beam undergoes arbitrarily large deformations. The modelling of these follower effects are an inherent part of the nonlinear modelling requirements of a highly deflected structure generating aerodynamic loads.

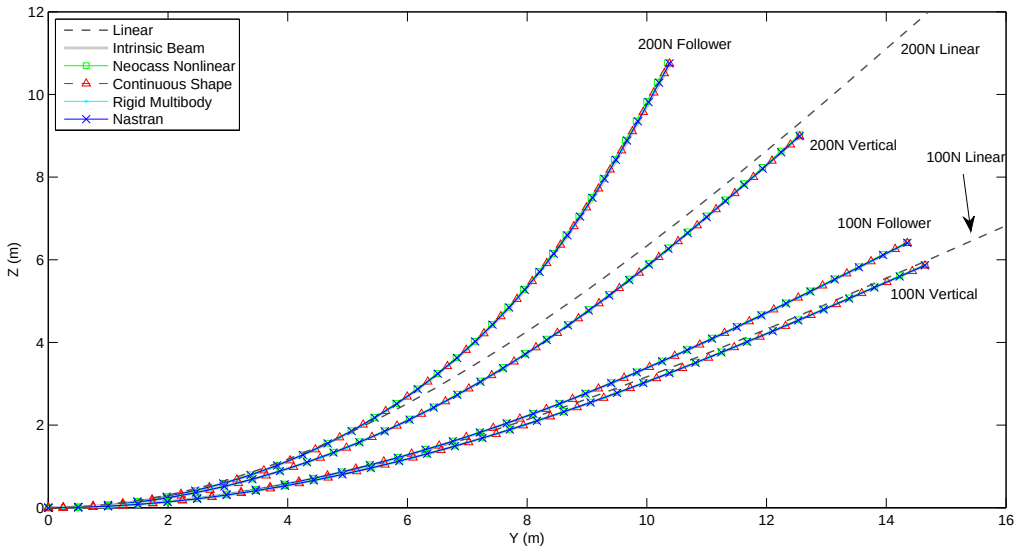


Figure 13: Predicted wing deflection from the five nonlinear modelling methods resulting from the application of 100N and 200N vertical and tip loads. The linear deflection is also given as the dashed lines.

The results for the four tip load cases are shown in figure 13 for each of the methods introduced in this work, along with the linear approximation. It can be seen for all four tip load cases that there is an excellent agreement between all the methods presented. The significant beam deformations, and consequent tip shortening effects, can be observed and are captured well by each approach. The linear results, which can only model a global, non-follower force, differ substantially from the nonlinear results, and illustrate the limitations of the linear approximation when considering highly flexible structures.

## III.B. Static Aeroelastic Comparison

### *III.B.1. Fixed root angle of attack cases*

In the following sections the aeroelastic results are now considered for the five different nonlinear modelling methods detailed in section II coupled to the aerodynamic methods of section II.G. At first spanwise distributions are shown of several quantities of interest, namely deflections in the global coordinate system, twist and aerodynamic forces. In each case the curves are shown for fixed root angles of attack of 1, 2, 5 and 10 degrees. The flight condition corresponding to these static tests is for an airspeed of 30 $m/s$ and air density $\rho = 0.0881\, kg/m^2$ (see table 1).

The deflected profile is considered first; figure 14(a) shows the global $Y$-$Z$ projection of the wing; 14(b) illustrates local angle of attack along the wing which provides a measure of wing twist. In both panels (a) and (b) one observes overall agreement between the different methods for smaller angles of attack with growing discrepancies visible between the predicted distributions for higher root angles of attack. In particular, the intrinsic-beam, continuous-shape and NeoCASS models show close agreement; the rigid-multibody nonlinear results show a slightly greater twist but smaller overall deflection for larger $\alpha$.

Of particular note is the Nastran $\alpha$ distribution of panel (b), the results of which deviate visibly from the other nonlinear methods for larger $\alpha$. As detailed in section II.G these differences stem from the geometric reference frame in which the Nastran aerodynamic loads are generated as well as the effects of linearisation for large $\alpha$. As seen in both figures 14(a) and 14(b) by matching these assumptions with the NeoCASS method (see the curves labelled Neocass –> Nastran) the Nastran result may be replicated.

In figure 15 the coefficient of lift distributions are compared between the five methods. As one might expect the continuous-shape, intrinsic-beam and NeoCASS methods, all employing VLM aerodynamics, yield very similar distributions. The rigid multibody formulation employing a strip theory aerodynamic description

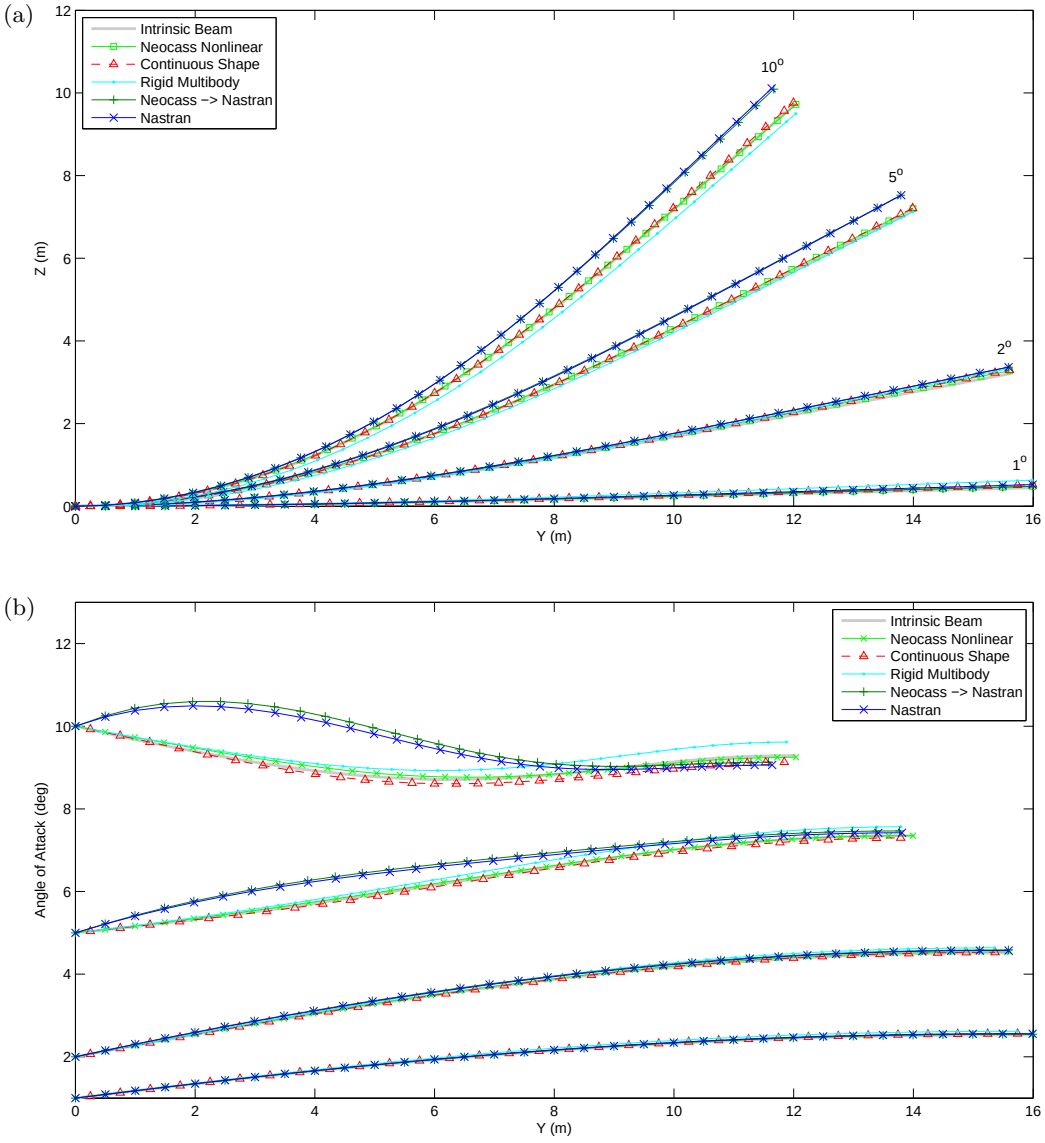


Figure 14: Aeroelastic results for fixed root angles of attack of 1, 2, 5 and 10 degrees. Panel (a) shows the vertical deflection and panel (b) the local angle of attack of the wing as the global Y position along the beam is varied.

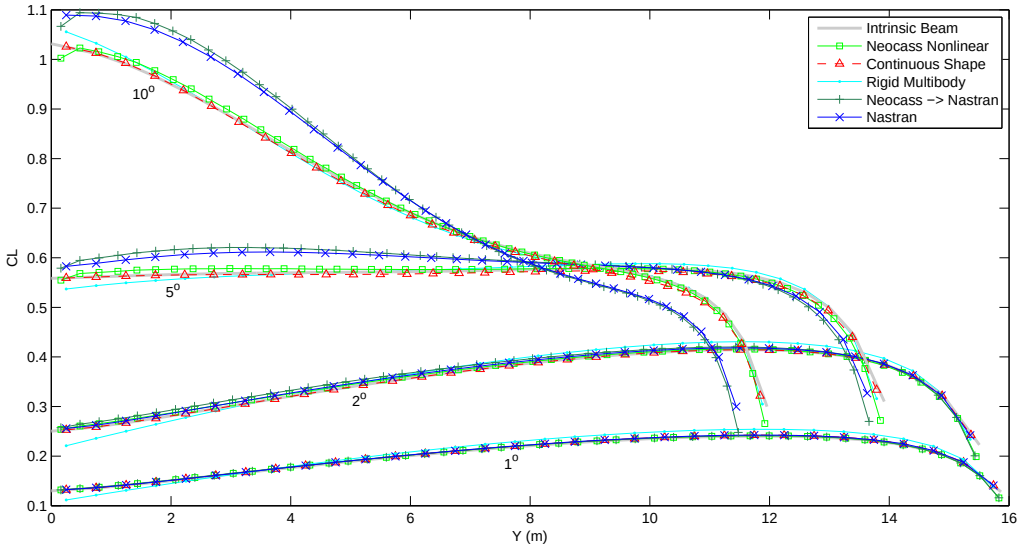


Figure 15: Aeroelastic results for fixed root angles of attack of 1, 2, 5 and 10 degrees. Shown here is the coefficient of lift distribution along the wing as a function of the global position Y.

predicts a slightly different result although overall agreement is still very good. The Nastran and modified NeoCASS methods produce similar distributions but distinctly differ from the other nonlinear methods for higher root angles of attack. Note that the larger CL values towards the root are reflected by the higher in-board $\alpha$ angles observed in figure 14(b).

### *III.B.2. Quantities of interest vs angle of attack*

Overall the results between the modelling methods given in the previous sub-section show the prediction of similarly shaped spanwise distributions of deflection, twist and aerodynamic loading with quantitative differences accumulating at increasingly high root angles of attack where geometric nonlinear effects are more significant. These findings are used to motivate the results of this section. Specifically, here we examine the overall trends in a number of quantities of interest as the angle of attack and consequently the magnitude of geometric nonlinearity is increased. Linear results are also shown in each case against which the nonlinear trends are compared. The particular quantities of interest considered are the vertical tip displacement, total lift, root bending moment and root twist moment. These are shown in panels (a)-(d) of figure 16 respectively.

The vertical tip displacement curves of panel (a) may be compared to figure 14(a). As the previous result indicates, the rigid-multibody nonlinear results give slightly lower predicted tip deflections of the wing as $\alpha$ increases when compared to the continuous-shape, intrinsic-beam and NeoCASS methods; Nastran predicts the highest deflections with the adapted NeoCASS curves matching this result. The linear curve, which lies above these results, is observed to deviate substantially from the nonlinear curves, greatly overestimating the magnitude of tip deflection for the higher $\alpha$ test cases.

A similar over-prediction by the linear result is observed in panel (b) this time treating the net lift produced over the entire wing. Here the nonlinear methods instead display a gradual reduction in the generated lift-per-$\alpha$. The reason for this gradual levelling of the curves is geometric and relates to the increasingly large inboard component of the aerodynamic forces generated along the wing. In essence the wing becomes less efficient at generating useful lift for the larger structural deflections that result at higher angles of attack. In fact for the flexible wing detailed in this paper it is not possible to trim the aircraft to a 2g trim condition (the full aircraft model[17] having a mass of 74.4 kg).

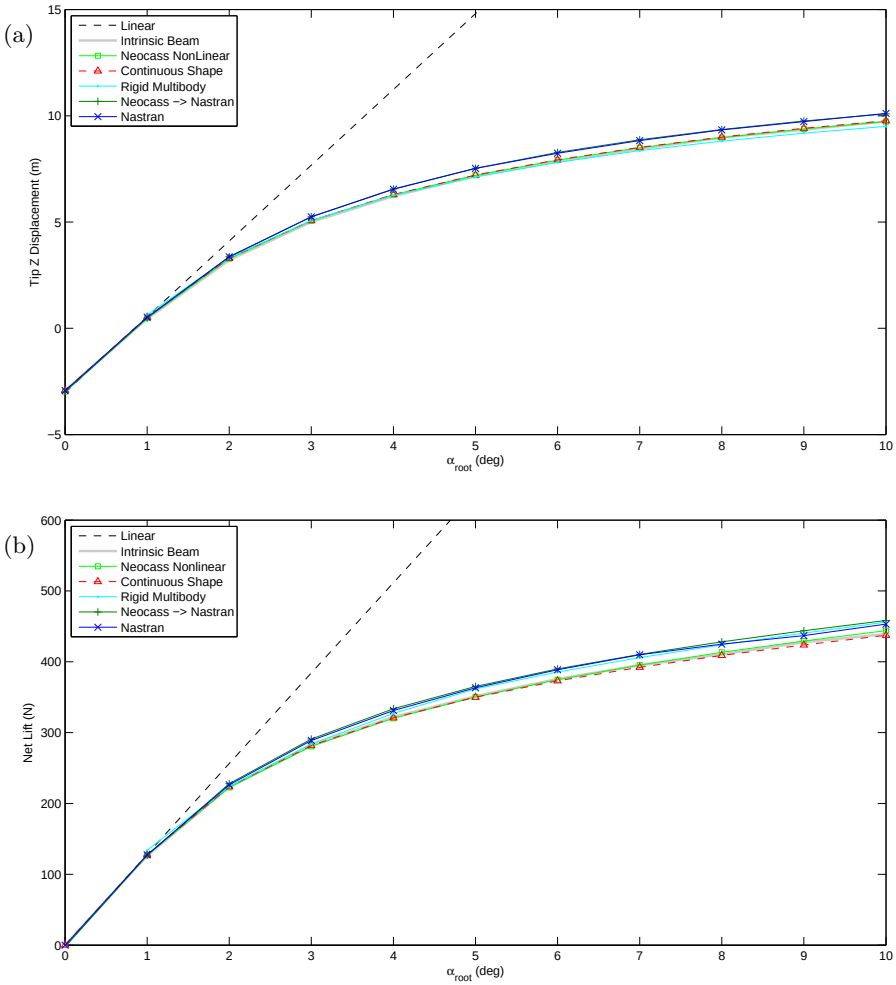


Figure 16: Aeroelastic static trends as root angle of attack is varied. Panel (a) shows the variation in vertical tip deflection and panel (b) the net lift produced by the wing.

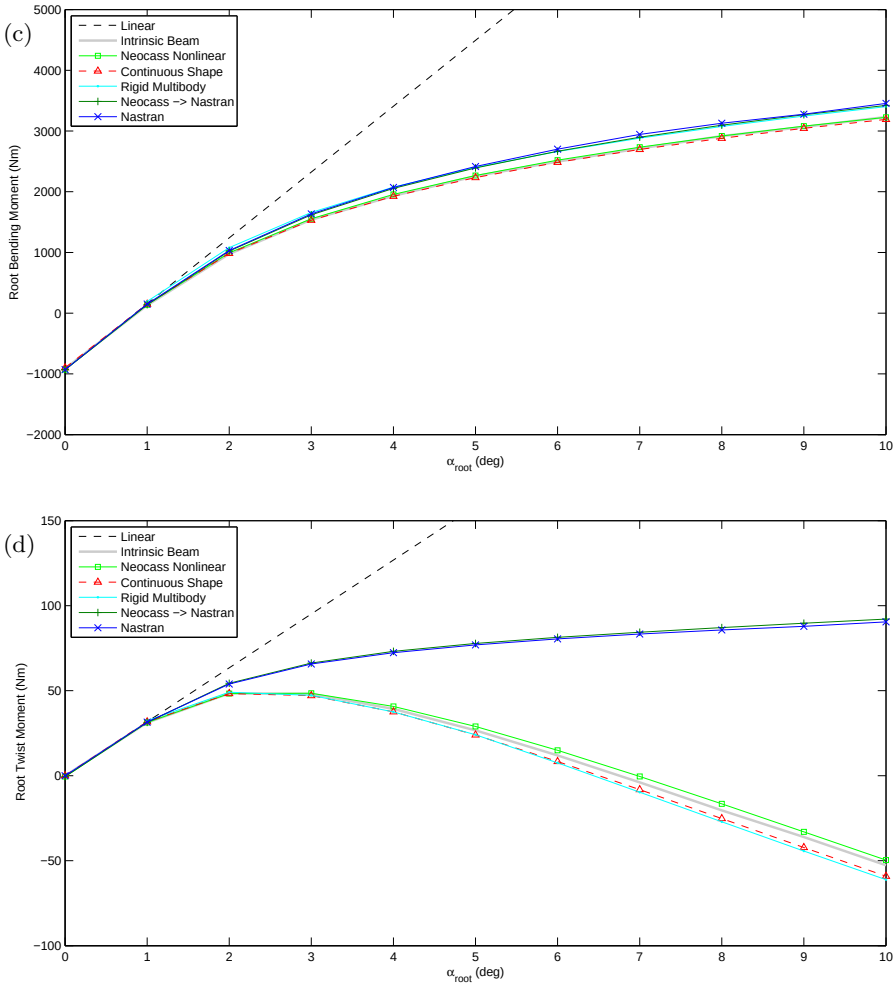


Figure 16: Continued . . . panels (c) and (d) show the variation in root bending moment and root bending twist respectively, as the root angle of attack is varied.

The root bending and twist moments of panel (c)-(d) show similar diminishing trends. Once again the linear results greatly overestimate the magnitude of these root moments. Some separation between the Nastran and other results are seen in panel (c), however these differences are vastly more evident in the root torque plot of panel (d). Here the different geometric treatments of the aerodynamic forces lead to very different root twisting moment trends. To explain these differences reference is made back to figure 12 detailing the geometric orientation of aerodynamic forces. One recalls that for the Nastran aerodynamic implementation all aerodynamic forces are cast in the global reference frame in the (Y,Z)-plane with no X component (this being a consequence of the linearisation of the incoming flow direction). For the other models, the lift generated is cast perpendicular to the free-stream velocity. In the global frame this force orientation gives a forward component to the aerodynamic force which in turn produces a negative (pitch down) component to root twist; hence leading to the lower set of curves observed in panel (d).

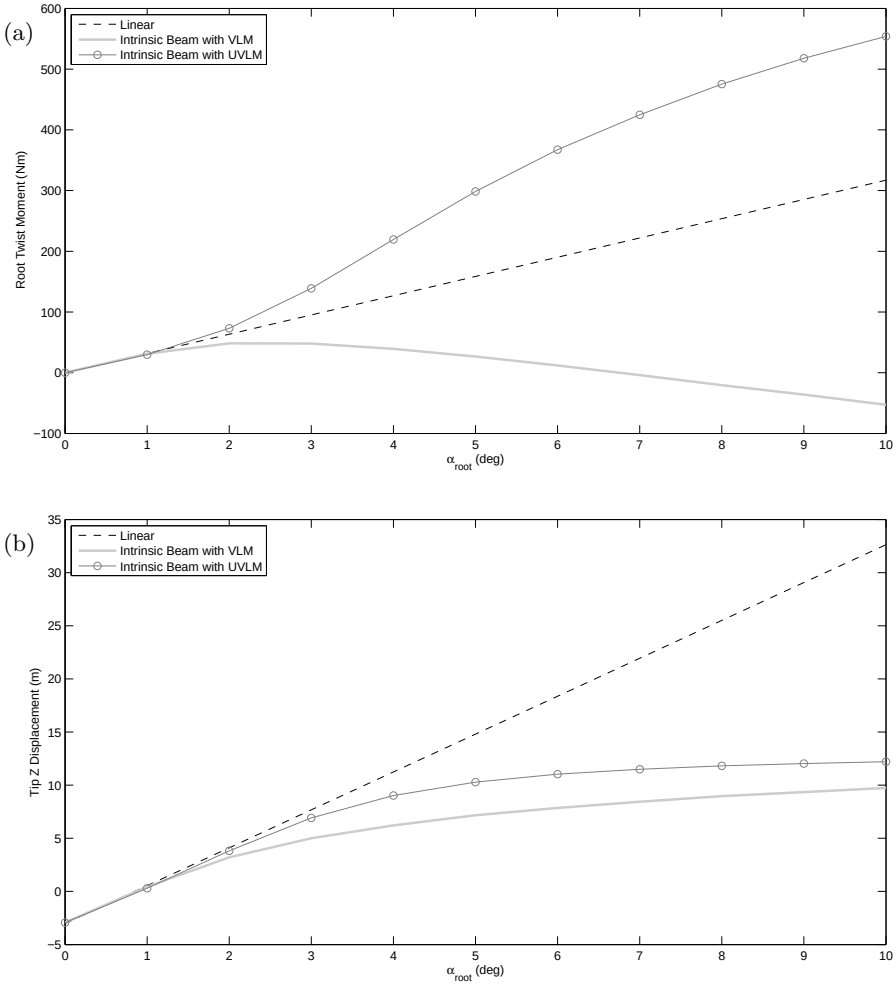


Figure 17: Variation in twisting moment (a) and vertical tip displacement (b) as $\alpha$ is varied. Results are shown for the intrinsic beam model both with drag (using UVLM aero) and without drag (using VLM).

It is worth noting here that neither situation is truly correct as in practice drag effects (not modelled by the aero methods detailed thus far) would dominate this root twist moment for higher deflected wing profiles, producing a strong pitch up moment to counteract the trends observed above.

To capture this effect and briefly illustrate the influence of drag forces on the results, a small selection of figures is replotted using the intrinsic beam model combined with an unsteady VLM (UVLM) aerodynamics method. This UVLM method calculates an additional drag component which is not accounted for in

the VLM and DLM (though it should be noted that the particular UVLM code used here does not model leading-edge suction and as a result over-predicts drag a little). The root twisting moment generated by both aerodynamic implementations is shown in figure 17(a); the VLM, UVLM and linear methods are shown to each predict very different results with the UVLM aerodynamics producing the largest moments. Physically, the UVLM added drag components are acting over the vertical moment arm between the point of force application and the wing root, hence explaining the increasingly large pitch up moment observed as the angle of attack (and therefore wing deflection) increases. Figure 17(b) shows the tip displacements for a selection of angles of attack, again using both VLM and UVLM codes. It can be seen that the increased pitch up moments generated by the aforementioned drag components increase the overall tip displacement by a considerable amount. These results therefore highlight the potential impact of drag modelling on the predicted static results and motivate the inclusion of drag effects in future work.

## IV. Conclusions

This paper demonstrates that the assumptions made in performing a linear analysis can lead to significant errors in predicted deflections and loads when treating a highly flexible wing. Here, the primary sources of nonlinearity driving these differences are the substantial geometric effects of a largely deflected structure. Increasing the root angle of attack of the flexible wing considered strengthened the influence of these effects resulting in larger differences between linear and nonlinear results. Particular trends observed from the linear results across the test cases were: a consistent over-estimation of wing deflection, bending moment, net lift and large differences in twisting moment (positive/negative depending on the inclusion of drag effects). For an aeroelastic analysis these nonlinearities influence all aspects of system performance. Hence, modelling techniques capable of capturing suitable forms of nonlinearity are required to effectively represent systems in which these effects may no longer be considered 'weak'.

In this paper five such nonlinear modelling techniques were discussed and a comparative analysis performed comparing their predictions of static aeroelastic equilibria. Altogether, each method successfully incorporated nonlinear effects important to this class of flexible wing design. In particular, good agreement was observed between the continuous-shape, intrinsic-beam and NeoCASS methods. This finding reflects the similar structural deflection results and implementation of equivalent VLM aerodynamics. All three of these methods have the advantage of being quick to run (particularly the continuous-shape and intrinsic beam formulations; typically in the region of 10 seconds per static test) and are all expandable to treat more complex geometric cases. The rigid multibody method also gives similar advantages in terms of run time and structural representation, however, the results generated by this method throughout the paper showed differences when compared to the previous three methods. These differences stem from the required implementation of strip theory aerodynamics, a limitation which would need to be relaxed in future comparative analyses. Finally, the Nastran method demonstrated the largest difference in predicted results, however these are also similarly explained via consideration of the aerodynamic implementation. Specifically, via adaptation of its aerodynamic code, the NeoCASS method was able to switch agreement between the Nastran and other nonlinear methods. Hence the imposition of linear aerodynamics is a key limitation of the Nastran method detailed here; however, one may possibly circumvent this limitation through incorporation of an independent aerodynamic code coupled to the current aeroelastic solution strategy. Achieving this would combine the benefits of a nonlinear aeroelastic analysis with the modelling flexibility and validated architecture of Nastran but at the expense of additional run time when compared to the previous methods. Finally, the observed aerodynamic sensitivity of the static examples presented here also pointed to the importance of suitable drag modelling in the flexible aeroelastic problem; several illustrative examples that included drag indicated the necessity of its inclusion in future analyses. It is the intention of future work to further compare these methods against the results of a experimental test campaign of an example high aspect ratio flexible wing.

An additional point to note is that in practise it is feasible that specific attributes of all of these methods may be brought together into a suitable framework to produce an overall nonlinear design strategy. For example, optimisation methods may seek the optimal values for numerous structural parameters pertinent to a full 3D wing design e.g. rib orientation, box section properties. However, such optimisation runs are often computationally intensive. The ability to reduce such problems to a 1D characterisation for the determina-

tion of certain key performance criteria (e.g. root loads, flutter boundaries) holds the potential to drastically reduce the run time of such design problems. Hence the synthesis of traditional high fidelity modelling and efficient reduced order nonlinear models forms an important avenue of continuing research.

## V. Acknowledgements

The research leading to these results has received funding from the InnovateUK Agile Wing Integration Project (TSB-113041) and the European Community's Marie Curie Initial Training Network (ITN) on Aircraft Loads Prediction using Enhanced Simulation (ALPES) FP7-PEOPLE-ITN-GA-2013-607911. Simon Neild is also supported by an EPSRC fellowship (EP/K005375/1) and Jonathan Cooper holds a Royal Academy of Engineering Research Chair.

## References

[1]The Airbus Concept Plane. www.airbus.com/innovation/future-by-airbus/the-concept-plane/the-airbus-concept-plane.

[2]LMS Virtual.Lab 13.1, accessed June 2014. www.plm.automation.siemens.com/en_gb/products/lms/virtual-lab/13-1.shtml.

[3]Timothy J. Allen, Bradley W. Sexton, and Matthew J. Scott. SUGAR Truss Braced Wing Full Scale Aeroelastic Analysis and Dynamically Scaled Wind Tunnel Model Development. In *56th AIAA/ASCE/AHS/ASC Structures, Structural Dynamics, and Materials Conference*, Kissimmee, Florida, 2015.

[4]Bottasso C. L. Bauchau, O. A. and Y. G. Nikishkov. Modeling rotorcraft Dynamics with Finite Element Multibody Procedures. *Mathematical and Computer Modelling*, 33:1113–1137, 2001.

[5]O. A. Bauchau. *Flexible Multibody Dynamics, 1st ed.* Springer, Dordrecht, Heidelberg, London, New York, 2010.

[6]L. Cavagna, S. Ricci, and L. Riccobene. A fast tool for structural sizing, aeroelastic anlysis and optization in aircraft conceptual design. In *50th AIAA/ASME/ASCE/AHS/ASC structures, structural dynamics, and materials conference*, number AIAA Paper No. 2009-2571, Palm Springs, CA, 2009.

[7]Masarati P. Cavagna, L. and G. Quaranta. Coupled Multibody/Computational Fluid Dynamics Simulation of Maneuvering Flexible Aircraft. *Journal of Aircraft*, 48(1):92–106, 2011.

[8]J. D. Connelly and R. L. Huston. The Dynamics of Flexible Multibody Systems-A Finite Segment Approach. I: Theoretical Aspects. *Computer & Structures*, 50(2):225–258, 1994.

[9]C. W. Gear. *Numerical Initial Value Problems in Ordinary Differential Equations.* Prentice-Hall, Englewood-Cliffs, NJ, 1971.

[10]G. L. Ghiringhelli, P. Masarati, and P. Mantegazza. A Multi-Body Implementation of Finite Volume Beams. *AIAA Journal*, 38(1):131–138, 2000.

[11]D. H. Hodges. A mixed variational formulation based on exact intrinsic equations or dynamics of moving beams. *International Journal of Solids and Structures*, 26(11):1253–1273, 1990.

[12]D. H. Hodges, X. Shang, and C. E. S. Cesnik. A doublet lattice method for calculating lift distributions on oscillating surfaces in subsonic flows. *Journal of the American Helicopter Society*, 41(9), 1996.

[13]D. H. Hodges, X. Shang, and C. E. S. Cesnik. Finite element solution of nonlinear intrinsic equations for curved composite beams. *Journal of the American Helicopter Society*, 41(9), 1996.

[14]W. R. Krüger. Multibody Dynamics for the Coupling of Aeroelasticity and Flight Mechanics of Highly Flexible Structures. In *Proceedings of the IFASD 2007*, Stockholm, Sweden, June 2007.

[15]W. R. Krüger and M. Spieck. Aeroelastics Effects in Multibody Dynamics. *Vehicle System Dynamics*, 41(5):383–399, 2004.

[16]R. Palacios, J. Murua, and R. G. Cook. Structural and aerodynamic models in the nonlinear flight dynamics of very flexible aircraft. *AIAA Journal*, 48(11):2648–2659, Nov 2010.

[17]Mayuresh J. Patil, Dewey H. Hodges, and Carlos E. S. Cesnik. Nonlinear Aeroelasticity and Flight Dynamics of High-Altitude Long-Endurance Aircraft. *Journal of Aircraft*, 38(1):88–94, 2001.

[18]Bartels E. Robert, Scott C. Robert, Timothy J. Allen, and Bradley W. Sexton. Aeroelastic Analysis of SUGAR Truss-Braced Wing Wind-Tunnel Model Using FUN3D and a Nonlinear Structural Model. In *56th AIAA/ASCE/AHS/ASC Structures, Structural Dynamics, and Materials Conference*, Kissimmee, Florida, 2015.

[19]A. Shabana. *Dynamics of Multibody Systems, 3rd ed.* Cambridge University Press, Cambridge, England, UK, 2010.

[20]N. Teunisse, P. Tiso, L. Demasi, and R. Cavallaro. Computational reduced order methods for structurally nonlinear joined wings. In *56th AIAA/ASCE/AHS/ASC Structures, Structural Dynamics, and Materials Conference*, Kissimmee, Florida, 2015.

[21]Wei Zhao, Rakesh K. Kapania, Joseph A. Schetz, John M. Coggin, Timothy J. Allen, and Bradley W. Sexton. Nonlinear Aeroelastic Analysis of SUGAR Truss-Braced Wing Wind Tunnel Model Under In-plane Loads. In *56th AIAA/ASCE/AHS/ASC Structures, Structural Dynamics, and Materials Conference*, Kissimmee, Florida, 2015.

[22]Z. Zhao and G. Ren. Multibody Dynamic Approach of Flight Dynamics and Nonlinear Aeroelasticity of Flexible Aircraft. *AIAA Journal*, 49(1):41–54, 2011.